Materials Chemistry and Physics 275 (2022) 125292

Contents lists available at ScienceDirect

Materials Chemistry and Physics

journal homepage: www.elsevier.com/locate/matchemphys

Fabrication of electroactive multi-layered polyazulene thin films by atmospheric pressure-vapor phase polymerization

Rahul Yewale, Pia Damlin *, Milla Suominen, Carita Kvarnström

Turku University Centre for Materials and Surfaces (MATSURF), Laboratory of Materials Chemistry and Chemical Analysis, University of Turku, FIN-20014, Turku, Finland

HIGHLIGHTS

- First report on ultra thin (36–117 nm) polyazulene films synthesized by AP-VPP.
- Elucidation of structure, nature of charge carriers, and non-linear doping.
- Structural engineering of conducting multi-layered PAz films (12–20 mS/cm).
- High capacitance (706.2 F/cm^3) PAz films with low bandgap (1.6 eV).

GRAPHICAL ABSTRACT

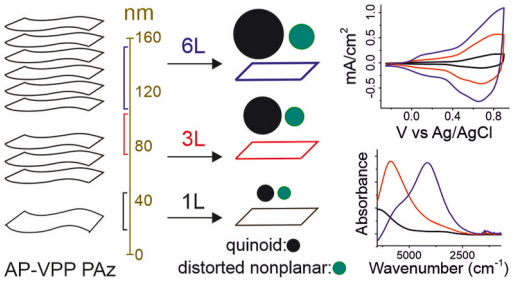

ARTICLE INFO

Keywords:
Polyazulene (PAz)
Atmospheric pressure-vapor phase polymerization (AP-VPP)
Thin films
Anomalous behaviour of PAz
Conducting polymer
Bandgap

ABSTRACT

Thin films of polyazulene (PAz) are produced by using an optimized atmospheric pressure–vapor phase polymerization (AP-VPP) method. Method optimization is carried out by studying the effect of cell temperature, substrate temperature, polymerization time, and washing-solvent on film properties like optical bandgap, sheet resistance, surface roughness, and % transmittance (%T). Multi-layered PAz films were produced by layer-by-layer engineering. The effects of thin, electroactive multiple layers on film properties are investigated. UV–Vis, IR, and Raman analysis are utilized to understand the extended conjugation length and nature of the charge carriers. The spectroscopic data revealed the anomalous behaviour of PAz at a high level of doping. The proportion and amount of quinoid conformation is discussed. The addition of layers changes the transport of ions across the electroactive PAz films, which is studied using cyclic voltammetry at various scan rates. AFM and SEM images reveal a change in structural properties which is further correlated with a deviation of capacitance values at elevated scan rate. Comparison with earlier reported literature on electrochemically and chemically synthesized PAz is also provided. The conductivity, transparency and high capacitance show a promising application of AP-VPP PAz in various fields.

1. Introduction

Azulene is a fused ring aromatic hydrocarbon consisting of an electron-rich five-membered and electron-deficient seven-membered ring that makes it a polarized entity. The electrochemical oxidation of azulene undergoes polymerization at 1- and 3- position to give 1,3-

* Corresponding author.
E-mail address: pia.damlin@utu.fi (P. Damlin).

https://doi.org/10.1016/j.matchemphys.2021.125292
Received 1 July 2021; Received in revised form 31 August 2021; Accepted 27 September 2021
Available online 27 September 2021

polyazulene [1]. Chemical polymerization of 1,3-dibromoazulene by using organonickel catalyst produced 1,3-polyazulene [2]. However, the on-surface synthesis approach via dehalogenative coupling of 2,6-diiodoazulene on Au(111) showed exclusive 2,6-connectivity [3]. The extended conjugation makes PAz a member of the conducting polymer family. PAz is p- as well as n-dopable conducting polymer showing fast charge-discharge behaviour. The electrochemical polymerization of azulene is well studied and evolved to the date [4–6]. To the best of our knowledge, there are only a few reports on chemical [2,7,8] and one report on photochemical [9] synthesis of PAz. The electrochemically synthesized PAz (Ele-PAz) shows conductivity values in the range of 1×10^{-3} to 1 S/cm [1,10,11]. It exceeded 4 S/cm in 5- or 6- isopropyl substituted azulene derived polymer [1]. The Ele-PAz film showed a conductivity of 2.2 S/cm [12], which must be an effect of substitution in azulene structure during electrosynthesis in borontrifluoride diethyletherate (Lewis acid). The chemically synthesized non-conducting PAz pellet exhibited a conductivity of 0.74 and 1.22 S/cm after being exposed to trifluoroacetic acid vapor for two days and iodine vapor for four days, respectively [2]. Grodzka et al. reported the highest specific capacitance of 400 F/g for electrochemically prepared PAz, whereas 120 F/g for the chemically prepared PAz [8,13]. Nöll et al. reported that theoretically the effective conjugation length of PAz is about 10, a band gap of 1.9 eV for infinite chain length, and a calculated band gap of 1.46 eV for chemically synthesized PAz [14]. PAz has been applied in batteries [4,15] and supercapacitor [6] due to its high capacitance and redox behaviour. It has been used as ion-to-electron transducer in calcium selective solid contact electrodes due to its high redox capacitance and hydrophobicity in an aromatic form (reduced form) [16]. The electronic properties and fast redox behaviour of PAz indicate that it is a promising material for electronics, antistatic coatings, dye-sensitized or organic solar cells, electrochemical transducers, electrochromic devices, electroluminescent devices, organic light-emitting diodes (OLED's), and supercapacitors. Despite its unique properties, PAz has not been studied as extensively as other conducting polymers such as polypyrrole and the polythiophene derivatives.

The electrochemical synthesis of PAz produces films with granular microstructures and film-thickness in the range of micrometers [6,16]. An increasing thickness of the film affects the transport of ions [13] in and out of the film, and the thicker films also become brittle. Electrochemical synthesis of PAz requires a substrate that is conducting limiting its fabrication only to such electrode materials [6,17]. Oxidative chemical synthesis of PAz produces the polymer material in powder or granular forms [8]. Further casting or processing is not possible due to the insoluble nature of PAz though the PAz-Br_2 complex shows partial solubility in selective organic solvents [7]. A new synthesis approach is needed in order to ease the processability of PAz with improved properties.

The vacuum-vapor phase polymerization (VPP) technique is well known for the synthesis of poly (3,4-ethylenedioxythiophene) (PEDOT), but it requires a sophisticated reactor equipped with processing gas and vacuum generator [18]. In contrast, atmospheric pressure based vapor phase polymerization (AP-VPP) needs a simple cell setup, it is fast, and, produces relatively superior thin films of PEDOT [18]. Earlier, we reported an AP-VPP technique for the production of highly conducting PEDOT films [18]. In the AP-VPP method, an oxidant-coated substrate is exposed to monomer-vapor at atmospheric pressure to form a thin layer of the polymer. It is further annealed to avoid stress-fracture, and, washed and dried to get rid of the excess amount of oxidant, unreacted monomer, reaction by-products, and, soluble species. In present work, we report a simple, fast, and cheap way of producing PAz thin films via AP-VPP. So far, this is the first report on the azulene polymerization by using AP-VPP. The method enables engineering of PAz films on different types of substrates at nanometer to micrometer scale. The AP-VPP PAz films prepared on microscope-glass slides and fluorine doped tin oxide (FTO) glass pieces are presented in this report. The method also allows the synthesis on bendable substrates. AFM and SEM provided the thickness and structural properties of the film surface. UV–Vis, IR, and, Raman analysis were utilized to understand the chemical nature and transparency of the produced films. Cyclic voltammetry measurements provided the information on electroactivity of the films. Dependence of the PAz film properties on the number of layers of PAz has been discussed. The AP-VPP PAz films produced in this work have been compared with literature data of electrochemically and chemically produced PAz. The effect of method parameters on the quality of the films has been briefly discussed. Such information would allow users to enhance the polymer properties like transparency, sheet resistance/-conductivity, surface roughness, and thickness. The sheet resistance behaviour helps to elucidate a change in the band gap of the films.

2. Experimental

2.1. Materials

Tetrabutylammonium tetrafluoroborate (TBA-BF_4) (99 %), azulene (99 %) and ferrocene (98 %) were purchased from Sigma-Aldrich. Copper (II) chloride dihydrate (99–101 %) ($CuCl_2$) from J. T. Baker was dried in vacuum oven. Hydrogen peroxide (30 %) (H_2O_2) and ammonium hydroxide (25 %) (NH_4OH) were purchased from Analer Normapur and J.T. Baker, respectively. *n*-Butanol (AR grade) and pyridine (AR grade) were obtained from Lab-scan analytical sciences. Acetonitrile (MeCN) (anhydrous, 99.8 %) was obtained from VWR chemicals. Ferrocene, azulene, *n*-butanol, H_2O_2, and NH_4OH were used without further purification. $TBABF_4$ was dried in vacuum oven at 75 °C for 2 h before use. MeCN was dried using molecular sieves (4 Å, Sigma-Aldrich) for more than 24 h prior to electrochemical characterization.

2.2. VPP method at atmospheric pressure for layer-by-layer preparation of PAz films

The substrate cleaning procedure [18] is specified in the supporting information. $CuCl_2$ oxidant solution of 240 mM concentrations were prepared by using *n*-butanol as a solvent. 80 μl of this oxidant solution was spin-coated on the substrate at 2400 rpm for 20 s. The oxidant-coated substrate was dried on a hot plate at 90 °C for 90 s. The dried substrate was immediately transferred to a preheated cell (Fig. 1) containing azulene monomer at 57 °C in such a way that the coated surface faced down towards the vapor. (The cell is not flushed with

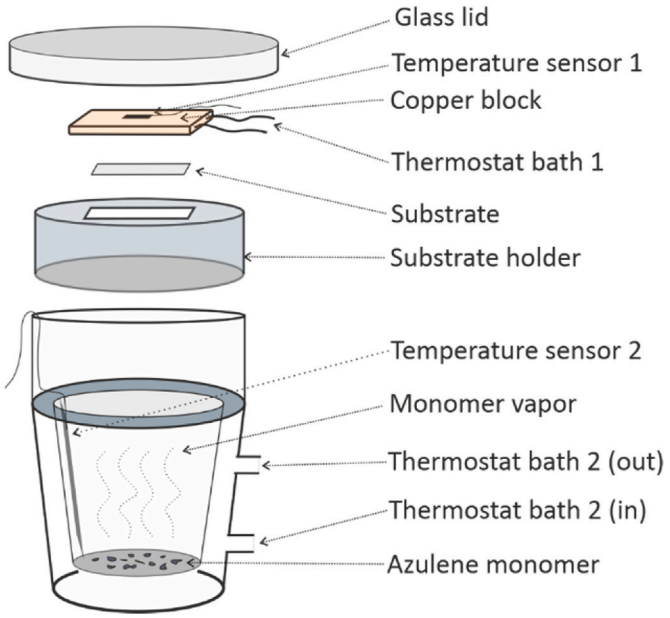

Fig. 1. AP-VPP cell.

nitrogen or any other gas). Polymerization was carried out for 4 min. After polymerization, the film was let to cool to room temperature and dip rinsed thoroughly two times in MeCN to remove unreacted oxidant, monomer, and, other by-products of the reaction. After washing, the film was dried under dry nitrogen gas stream. The procedure was repeated from the spin coating step to produce multilayers of PAz on the substrate. Thermostat baths controlled the temperature of the cell. Additional information found in literature about the enthalpy of sublimation and vapor pressure of azulene below its melting point has been provided in the supporting information (Tables S3 and S4).

Following conditions were applied while optimizing the method parameters: a) the polymerization time was 4 min, and the copper block controlling the substrate temperature was removed while optimizing the cell temperature. **b)** While conducting various substrate temperature experiments, the cell temperature was 57 ± 2 °C, and the polymerization time was 4 min. **c)** While running various polymerization time tests, the cell temperature was 57 ± 2 °C and the copper block controlling the substrate temperature was removed. (Note: The substrate temperature reported here is the temperature of the copper block in Fig. 1, which controls the temperature of the substrate. The maximum error in the temperatures reported in this work could be ±2 °C).

2.3. Characterization

Agilent 8453 spectrometer was used to record UV–Vis spectra of AP-VPP PAz films on glass substrate (background correction was done using an uncoated microscope glass slide). The optical bandgap is determined with a tangential through the onset of the absorption spectrum [14,19]. The IR spectra of AP-VPP PAz films on FTO glasses were recorded by Bruker Vertex70 FTIR spectrometer using a Harrick Seagull variable angle reflection accessory and liquid nitrogen cooled MCT detector at 70° angle of incidence relative to the surface normal. Spectra were recorded in the region 6500–700 cm^{-1} with 4 cm^{-1} spectral resolution. For each spectrum, 256 scans were averaged. Renishaw Qontor inVia Raman microscope equipped with Leica microscope, a CCD detector, 20X objective, 1200 and 1800 l/mm grating, and excitation source (λ_{exc}) of 532 nm and 785 nm was used to record Raman spectra at room temperature.

The sheet resistance (ρ_{sheet} in 'Ω/sq') of AP-VPP PAz films on glass substrate were determined by utilizing Jandel RM3000+ test unit in combination with a multi height 4-point probe with tip radius of 500 μm. The specific resistance (ρ) is obtained by multiplying sheet resistance in 'Ω/sq' with film thickness (d in 'cm') estimated by AFM. The conductivity (σ) is the inverse of its specific resistance (ρ).

Specific resistance (ρ) = [sheet resistance (ρ_{sheet} in 'Ω/sq') × film thickness (d in 'cm')]

Conductivity (σ in 'S/cm') = [1/(ρ)] = 1/[sheet resistance (ρ_{sheet} in 'Ω/sq') × film thickness (d in 'cm')]

Conductivity in 'S/cm' is converted into 'mS/cm' by multiplying 1000.

AFM measurements were carried out using Veeco diCaliber scanning probe microscope operated in a tapping mode at room temperature. All AFM images were recorded using Bruker TESP-MT probe (resonant freq. 320 kHz, spring const. 42 N/m, length 125 μm, width 30 μm, Cantilever spec: 0.01–0.025 Ωcm Antimony (n) doped Silicon, 4 μm thick, tip spec: 10–15 μm height, 8 nm radius). WSXM software [20] was used to determine root mean square of the roughness (RMS roughness) of AP-VPP PAz films. The thickness of the films in Table S1 is the average of the six measurements across the cut.

Electrochemical characterization was carried out by cyclic voltammetry in a conventional 3-electrode configuration using one-compartment Teflon cell specially designed for FTO glass substrates in 0.1 M TBA-BF_4/MeCN. PAz films synthesized by the AP-VPP method on FTO glass were used as working electrodes with area of 1.13 cm^2. An Ag/AgCl wire and a platinum wire were used as pseudo reference electrode and counter electrode, respectively. The reference electrode was calibrated before and after every electrochemical measurement using ferrocene redox couple ($E_{1/2}$ (Fe/Fe^+) = 0.46 V). Cyclic voltammograms (CV's) were recorded using Metrohm Autolab PGSTAT 101 potentiostat in a potential range from −0.25 V to 0.9 V against reference electrode using the scan rates of 20, 50, 100, 150, and 200 mV/s. The charge (Q) is calculated by integration of the CV in the potential range −0.25 V–0.9 V in the Origin software, which is further processed by using following equations to obtain capacitance values:

Areal capacitance, $C_A = Q/(\Delta V \times A)$

Volumetric Capacitance, $C_V = Q/(\Delta V \times V)$

Where, 'ΔV' is the potential window, 'A' is the area and 'V' is the volume of working electrode. In areal capacitances, three results have been considered for the estimation of charge values. For volumetric capacitances, three results have been used to estimate charge values, and six results have been considered for the thickness of the films. The error has been reported as standard deviation (Std Dev) and relative standard deviation (RSD in %) in Table S2.

(Note: All solutions were purged with dry nitrogen gas for 15 min prior to measurement).

3. Results and discussion

3.1. AP-VPP method parameters

In electrochemical polymerization, scan rate, potential window, concentration of the monomer, solvent, and, supporting electrolyte play an essential role in producing films with different properties [13,21]. Additionally, the temperature of the medium becomes important while using ionic liquids [22,23]. In chemical polymerization; temperature, time, solvent (used as reaction medium), and the oxidant become of vital importance in determining the yield and properties of the resulting polymer [2,7,8]. In AP-VPP PAz method, the cell is saturated with monomer vapor, which makes the concentration of the monomer a non-variable entity. The oxidant on the substrate is in the form of a thin solid film where mobility of oxidant molecules is frozen in the solid-state. The cell temperature, polymerization time, and the substrate temperature are the factors mainly determining the microstructures and the properties of the resultant polymer film [18]. These are the crucial parameters of the AP-VPP method. The type of washing solvents do not have a significant impact except that, the harsh washing solvents can destroy the film, and unsuitable solvent does not wash away the unreacted monomer, oxidant, and, by-products of the reaction which affect the film quality. This washing effect on the sheet resistance (SR) of the films is also studied in this work using MeCN and reported as before and after the washing, i.e. SR (BW) and SR (AW), respectively. Various concentrations of $CuCl_2$ in n-Butanol (oxidant solution) were tested, and films of high capacitances were obtained by using 240 mM oxidant solution. Hence, the same concentration of the oxidant solution was used for the optimization of the remaining synthesis parameters.

a) **Cell temperature:** (The polymerization time was 4 min and substrate temperature control was removed). At 25 °C, very thin and fragile (island connecting structures) PAz films are produced with very high sheet resistance which must be due to the insufficient amount of monomer vapor at low temperature (Fig. 2a). The AFM images (Fig. S1) and the increase in roughness (Fig. 3a) prove that increasing the cell temperature from 25 to 35 and further to 45 °C leads to fast deposition of the polymer. Further raising of the temperature until 85 °C leads to a slow but steady drop in roughness suggesting that the rate of deposition continues to grow and smoothens the roughness of the film. This smoothening could be due to the cross-linking of the polymer as a result of faster deposition at elevated temperatures. The sheet resistance (both BW and AW) and the band gap first decreased with raise in the cell temperature and then increased with high cell temperature. The PAz formed at cell

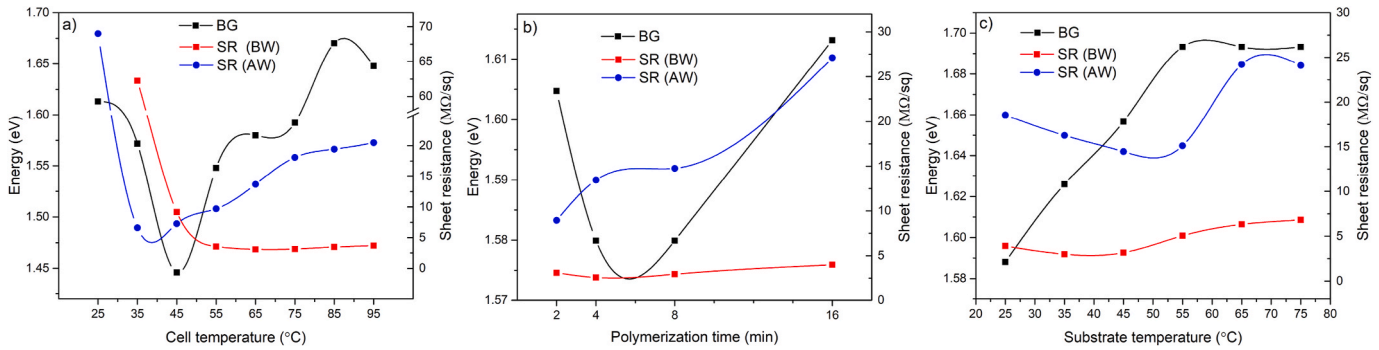

Fig. 2. The dependence of band gap (BG) and sheet resistance (SR) before washing (BW) and after washing (AW) of the one layered PAz film prepared at various **a)** cell temperature, **b)** polymerization time, **c)** substrate temperature.

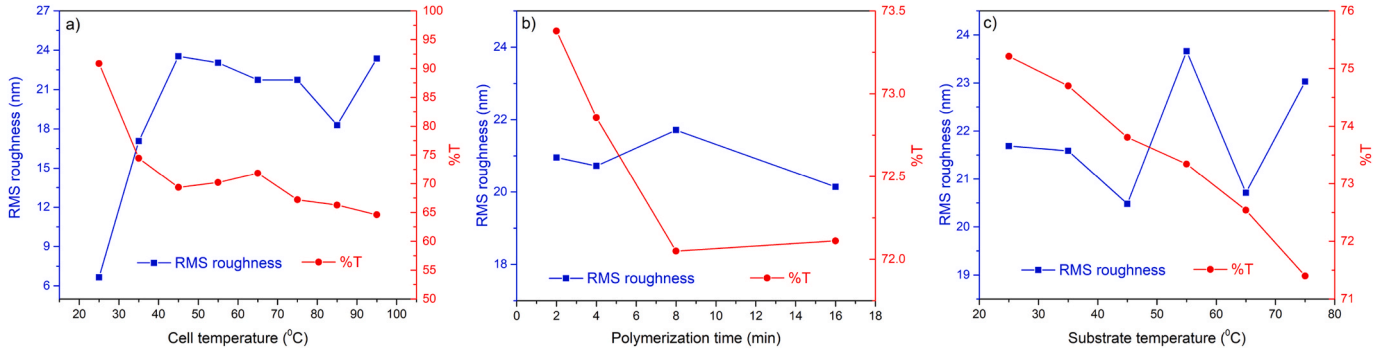

Fig. 3. Variation in surface roughness (RMS roughness in nm) and % transmittance at 550 nm (%T) of the one layered PAz film prepared at various **a)** cell temperature, **b)** polymerization time, **c)** substrate temperature.

temperatures of 35–45 °C showed a low sheet resistance and a low band gap. The increase in SR at high cell temperature could be due to the elevated polymerization rate at high temperature, causing extended cross-linking within the film, which would restrict the doping induced geometrical changes within the film. In Fig. 2a, the drop in BG from 25 to 45 °C must be due to successively extended conjugation/chain lengths in the PAz film. The BG increases from 45 to 65 °C and onwards except the change in the behaviour from 65 to 95 °C. The SR (AW) also increases from 45 °C onwards following nearly the same behaviour as the BG. The low BG and SR (AW) are complementary to each other but not justifying completely. SR (BW) reduces from 35 to 55 °C, whereas SR (AW) slightly increases from 35 to 55 °C. In contrast, the BG drops from 35 to 45 °C and increases from 45 to 55 °C. This anomalous behaviour can be explained by considering that the oligomers or short polymer chains are better conducting than the cross-linked polymer [14]. The amount of oligomers or short polymer chain formation at 35 °C increases at 45 °C and continue further at 55 °C resulting in the drop of SR (BW). After washing the PAz films in MeCN, the soluble part of oligomers or short polymer chains must have been swept away, which is giving a slight increase in SR (AW). The BG drops at 45 °C due to the extended conjugation/chain length but increases from 55 °C indicating the cross-linking of the short chains on account of fast reaction rate at the elevated cell temperature. Similar behaviour is also observed with polymerization time. Fig. 3a–c shows that the cell temperature significantly affects %T more than the polymerization time and substrate temperature.

b) **Polymerization time:** (The cell temperature was 57 °C and substrate temperature control was removed.) In Fig. 2b, an extension in polymerization time from 2 min to 4 min causes decrease in BG, which must be due to the extended conjugation of the polymer chains. Simultaneously, the SR (BW) drops slightly due to the formation of better-conducting (shorter) polymer chains, which are then washed away, giving an increment in SR (AW). The BG remains nearly the same at 8 min, indicating that the chemical nature of deposited-PAz remains the same, except that the increase in polymerization time causes additional polymer deposition. This additional deposition would create a crowding effect due to bulky 7-membered ring; restricting the doping induced geometrical changes leading to slight growth in both SR (BW) and SR (AW). Further expansion of polymerization time to 16 min would intensify this effect. This intensified effect must have concurred with extended cross-linking as the polymerization process is happening at the interface of solid-phase oxidant and vapor phase monomer limiting the PAz formation only to the interface thus expanded polymerization time would cause cross-linking. The increased BG and SR (Fig. 2b) and reduced RMS roughness value (Fig. 3b) at polymerization time of 8–16 min confirm this behaviour.

c) **Substrate temperature:** (The cell temperature and polymerization time were 57 °C and 4 min, respectively). The tendency in Fig. 2c, and Fig. 3c can be assessed by three factors, i) the rate of polymerization would increase with rising temperature resulting in fast deposition; ii) the inflow of monomer vapor to the surface would diminish with the rising temperature of the surface, leading to insufficient monomer concentration and short-chain formations (inverse condensation effect), iii) at relatively high temperature, more cross linking would take place. In Fig. 3c, factors i) and iii) are evidenced by the jumps in roughness, and factor ii) by consistent drop in %T. The synergistic effect of these three factors would be the faster deposition with highly cross-linked short chains of PAz films as the substrate temperature raises. It makes the BG surge with raising substrate temperature from 25 °C to 55 °C, remaining nearly the same during further elevation (Fig. 2c). The SR (BW) drops due to the formation of short polymer chains until 45 °C and then start to increase from 55 °C onwards due to the high cross-linking in short-

chain PAz films. This effect is more pronounced in SR (AW) as the washing takes away oligomers or soluble short-chain PAz.

3.2. UV–Vis and NIR spectra of multi-layered AP-VPP PAz films

According to literature [11,14,24], the UV–Vis spectra in Fig. 4a shows the absorption band centered around 450 nm, which arises from the neutral part of PAz. Another shoulder observed around 660 nm (and above) is due to the charge carriers' formation (polarons/bipolarons/polaron pairs) upon doping of the film. The increase in absorbance of the neutral band of PAz grows from 1L to 3L and further to 6L. Similar pattern is observed for the shoulder at 660 nm. It indicates that the PAz films prepared in this work by AP-VPP are in a partially oxidized form. Furthermore, the absorbance in the range 600 nm (16667 cm^{-1}) and 1100 nm (9091 cm^{-1}) (Figs. 4a) and 1538 nm–5000 nm (i.e. from 6500 cm^{-1} to 2000 cm^{-1} in Fig. 5b) confirms that the prepared-films possess a certain level of doping. Studies reported by Meana-Esteban et al. showed that while doping the electropolymerized PAz from −0.2 V to 1.1 V, two absorbance maxima were developed at around 3700 and 6200 cm^{-1} [5]. The 3700 cm^{-1} region dominated at low applied potential (low doping level) and 6200 cm^{-1} at higher potential (high doping level). Chemically or electrochemically doped PAz shows broad band absorptions in the range 4000–20000 cm^{-1} due to the formation of charge carriers between valence and conduction band [14]. Absorbance maxima of the radical cations and dications of electrochemically generated PAz (obtained by spectroelectrochemistry in the range between 4000 and 20500 cm^{-1}) at <4000, 12,000, 17700 cm^{-1} (at low doping) and 8000, 18600 cm^{-1} (at medium doping), respectively are reported by Nöll et al. [14]. For chemically synthesized PAz, absorbance maxima of the radical cations and dications are reported at 4300, 18600 cm^{-1} (at low doping) and 6000, 19400 cm^{-1} (at medium doping), respectively [14]. In the same studies, it was also observed that the absorbance maxima of radical cation shifted from 7000 cm^{-1} to lower energy (<4000 cm^{-1}) with an increase in the polymer chain length [14]. By utilizing DFT calculations on octaazulene model compounds, Nöll et al. reported that neutral to highly charged octamers' geometry optimisations led to a strongly distorted nonplanar structure [14]. In Fig. 5b, the 1L PAz shows absorption maxima around 6567 cm^{-1}, 3L PAz around 5900 cm^{-1}, and 6L PAz around 4137 cm^{-1} with an additional less intense band at 5600 cm^{-1}. According to the aforementioned reports, the bands in Fig. 5b must be due to the radical cations generated in the PAz films. The shift to lower energy with the addition of layers could be the combined effect of growing azulene units in polymer chains and the diminishing linear degree of doping.[1] Additionally, the reduction in BG from 1L to 3L and to 6L PAz (Fig. 4b) suggests the extended delocalization of the charge across the multiple layers. The improvement in charge delocalization with the reduction in doping degree would suggest and confirm that the PAz would acquire more planar conformation than the distorted nonplanar conformation [11,14,25] with the addition of layers. This simplification indicates that the 6L PAz should show lower sheet resistance values than the 3L PAz film and 3L lower than the 1L PAz, which goes very well with the results shown in Fig. 4c. The conductivity of the films drops slightly with the increasing number of layers due to the non-linear and inadequate drop in sheet resistance from 1L to 3L and to 6L PAz. The sheet resistance increases after washing due to the dissolution of the soluble oligomers.

3.3. IR spectroscopic characterization of AP-VPP PAz

Previous FTIR studies for electrochemically synthesized PAz (Ele-PAz) shows upon electrochemical doping absorption in the region from 2000 cm^{-1} which extends continuously over 7000 cm^{-1} indicating the formation of different charge carriers [5,14,23]. PAz prepared by AP-VPP shows absorbance maxima dominating in 2000–6500 cm^{-1} range. In Table 1 the IR vibrations observed for AP-VPP PAz (Fig. 5a) are compared with chemically (Che-PAz) [2,7,8] and electrochemically synthesized PAz [5,6,12,23] and are further discussed below. Data reported as PAz A to C and PAz D to H represent Che-PAz and Ele-PAz, respectively. PAz F and G represent doping induced vibrations of Ele-PAz [23]; symmetric vibrational modes are silent in the infrared spectrum of a polyconjugated pristine polymer, but introduction of charge carriers into the polymer backbone will cause a break in the symmetry, and the polymer chain will become polarized causing these vibrational modes to become infrared active, i.e. doping induced vibrations.

Out-of-plane ring deformation (γ_{op}) due to the =C–H of PAz: In Table 1, γ_{op}(=C–H) is reported at 704 cm^{-1} in electrochemically p-doped PAz (H [5]) at 1.1 V. For AP-VPP PAz, the same weak band showing red shift is observed at 696 cm^{-1} (1L and 3L) and 698 cm^{-1} (6L). Chemically dedoped Ele-PAz (D [12]) showed a band at 737 cm^{-1}, whereas electrochemically doped Ele-PAz [5,23] showed blue shift to 754, 879, and 951 cm^{-1}. These bands appear at lower energy in AP-VPP and Che-PAz compared to electrochemically doped Ele-PAz (Table 1), which suggests that the resultant AP-VPP PAz is in the moderately doped state. This also supports the elucidation presented in UV–Vis data. The appearance of γ_{op}(=C–H) as intense bands at high energy in highly doped form could be due to the high steric hindrance in the quinoid form due to the extended conjugation and bulky dopant anions [5] (hexafluorophosphate, PF_6^-, 73.0 $Å^3$) [26] compared to Cl^- (24.8 $Å^3$) in AP-VPP. The peak at 856 cm^{-1} in doped Ele-PAz (H [5]), is growing as a shoulder for 1L to 3L and 6L AP-VPP PAz, which indicate increased doping interaction. The overtone due to γ_{op}(=C–H) is observed at 1708 cm^{-1} for Ele-PAz (E [6]). It appears at lower wavenumber for AP-VPP PAz and even lower for Che-PAz (C [8]).

In-plane ring deformation (γ_{ip}) due to the =C–H of PAz: In Table 1, the γ_{ip}(=C–H) vibration is observed in Ele-PAz and AP-VPP PAz around 1020 cm^{-1}. The vibration at 1065 cm^{-1} in electrochemically doped Ele-PAz (H [5]) appeared at a lower energy in Ele-PAz (E [6] to G [23]). It was not found in AP-VPP PAz spectrum and Che-PAz spectrum, hence it must be a characteristic band for the Ele-PAz. The relative shifts in γ_{ip}(=C–H) vibrations can be observed in Table 1 for AP-VPP, Ele-, and, Che-PAz. Most of the peaks of γ_{ip}(=C–H) vibrations appear at nearly the same wavenumbers except those peaks in electrochemically doped (at 1.1 V) Ele-PAz (H [5]), which appears at higher wavenumber. The reason must be the same as for the γ_{op}(=C–H) vibrations, upon doping the extended conjugation would reduce the double bond character of the sp^2 carbon and induce the bond strength between sp^2 carbon and hydrogen.

Stretching vibrations (ν) due to C=C of PAz: The extended conjugation upon doping would give additional single bond character to double bonds leading to the appearance of respective ν(C=C) vibrations at lower wavenumber. The higher the degree of doping, the bigger is the shift to lower wavenumber. This effect can be observed in Table 1. It can be concluded that in Table 1, the conjugation length or effect is highest in the Ele-PAz that is electrochemically doped at 1.1 V (H [5]) compared to Ele-PAz. The Che-PAz has the lowest conjugation effect, whereas AP-VPP PAz shows a moderate effect. Among the AP-VPP PAz, this extended conjugation length is relatively effective in 6L than the 3L, and in 3L than the 1L. This observation supports the extended delocalization of charge observed in UV–Vis data.

3.4. Raman analysis of AP-VPP PAz films

Raman spectra of AP-VPP PAz films obtained by using laser excitation wavelength of 532 nm ($\lambda_{exc} = 532$ nm) for azulene, 1L, 3L, and, 6L PAz are shown in Fig. 6a and b. The λ_{exc} = 532 nm should provide more information on the neutral segments of PAz as the excitation wavelength is associated more with the electronic transitions in

[1] Note: Linear degree of doping is defined as, if the 1L PAz is doped to 1 unit, then 3L and 6L PAz should show respectively 3 and 6 units of doping degree.

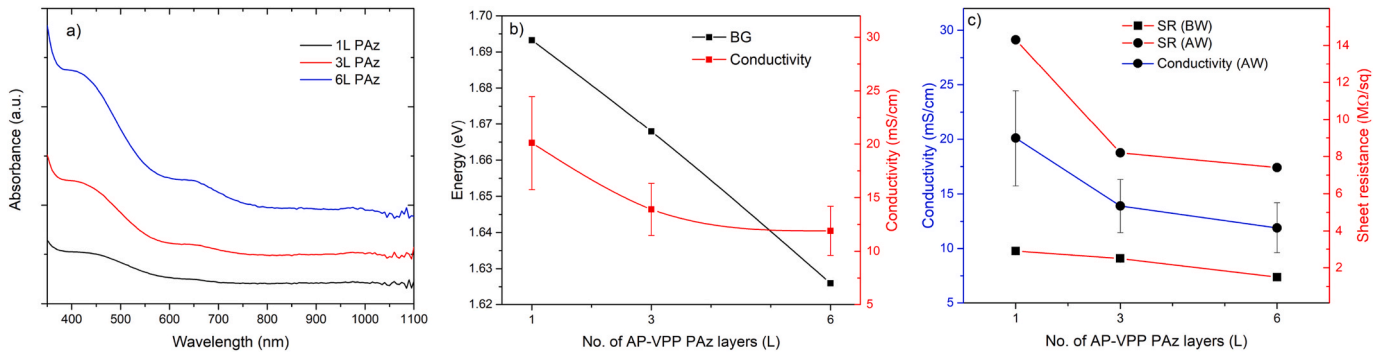

Fig. 4. **a)** UV–Vis spectra, **b)** BG and conductivity of the 1 layer (1L), 3 layers (3L), and 6 layers (6L) of AP-VPP PAz films on glass. **c)** Conductivity (AW), SR (BW), and SR (AW) of the 1L, 3L, and 6L AP-VPP PAz films on glass.

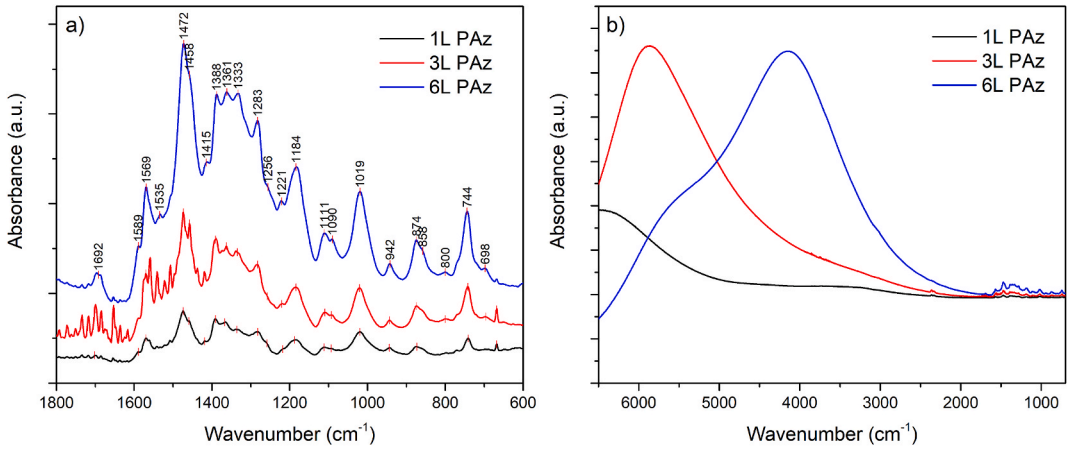

Fig. 5. IR spectra of the 1L, 3L, and 6L AP-VPP PAz films in the range **a)** 1800 to 500 cm^{-1} and **b)** 6500 to 700 cm^{-1}.

Table 1
Comparison of IR peaks (in cm^{-1}) found in 1L, 3L, and, 6L PAz (AP-VPP, present work) and IR data reported in the cited references (Vibrations: ν - stretching; γ - deformation; ip - in-plane; op - out-of-plane).

	AP-VPP PAz (present work)			Chemically Synthesized (Che-PAz)			Electrochemically synthesized (Ele-PAz)				
Vibrations	**1L PAz**	**3L PAz**	**6L PAz**	**A**[7]	**B**[2]	**C**[8]	**D**[12]	**E**[6]	**F**[23]	**G**[23]	**H**[5]
γ_{op}(=C-H)	696	696	698								704
	741	742	744		734	741	737	740	752	752	754
	855	856	858								856
	873	874	874					877	879	879	879
	944	944	942					945			951
γ_{ip}(=C-H)	1020	1021	1019				1020	1022			
								1056	1053	1053	1065
	1094	1093	1090								
	1111	1110	1112					1136			
	1187	1184	1184	1180				1190	1190	1188	1196
	1218	1221	1221	1220				1218		1220	1228
	1259	1258	1256							1253	1269
	1282	1283	1283	1290			1287	1290			
ν(C=C)	1336	1335	1333	1320				1328		1307	1308
	1367	1363	1361			1376		1348	1344	1357	1367
	1391	1391	1388		1395		1388	1394			
	1459	1458	1458	1450		1460		1452	1427	1413	1423
	1474	1473	1472	1465				1475	1473	1469	1493
	1570	1570	1569		1565	1573	1570	1566	1589	1591	1514
γ_{op}(=C-H)	1701	1695	1692			1690		1708			
						1681					

Note: ***C*** *– micro to nanostructures of Che-PAz,* ***D*** *– Chemically dedoped Ele-PAz,* ***F & G*** *– doping induced vibrations of Ele-PAz,* ***H*** *– Ele-PAz p-doped at 1.1 V.*

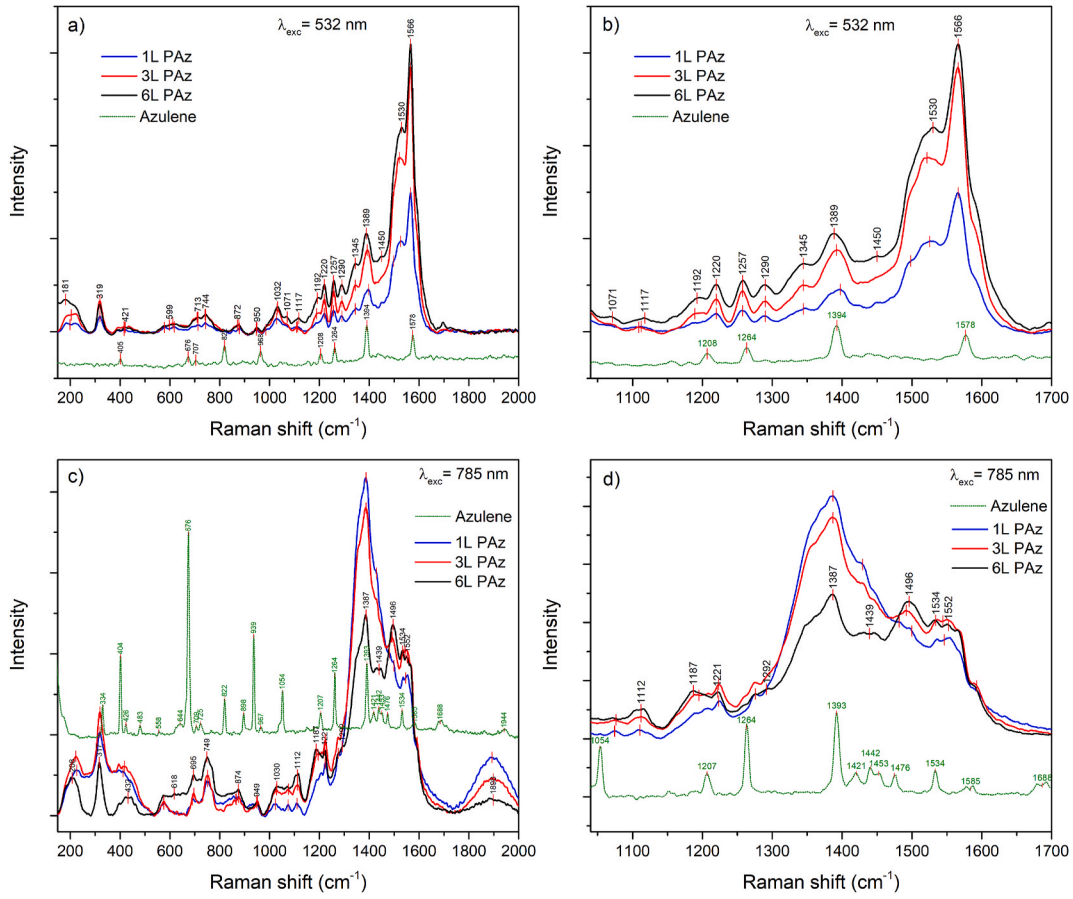

Fig. 6. Raman spectra of the 1L, 3L and 6L AP-VPP PAz films and azulene (powder) measured using λ_{exc} and measurement range of **a)** 532 nm (150–2000 cm^{-1}) **b)** 532 nm (1040–1700 cm^{-1}), **c)** 785 nm (150–2000 cm^{-1}) and **d)** 785 nm (1040–1700 cm^{-1}).

the neutral state of the PAz (resonance enhancement) (Fig. 4a) [5,27]. Many additional broad bands are developed in the polymerized state in comparison to azulene monomer. According to the *in situ* studies reported for Ele-PAz by Österholm et al. [27], additional bands are due to the PAz in a partially p-doped state. When comparing to Österholm's work, the spectrum at 0.6 V shows broadening of peaks similar as in 1L PAz. In Fig. 6a, the peak in the azulene spectrum at 1578 cm^{-1} shifts to 1566 cm^{-1} in the polymerized state. The peak at 1566 cm^{-1} does not grow linearly for 1L to 6L PAz. Intensity is very strong for 6L, it drops for 3L, and it further drops heavily for 1L PAz. It has a direct relation with the increment in the thickness from 1L to 3L and from 3L to 6L PAz (Table S1). In 1L PAz, the broad band at 1525 cm^{-1} (with a shoulder at 1498 cm^{-1}) shifts to 1522 cm^{-1} (with a weak shoulder at 1502 cm^{-1}) in 3L, which further shifts to 1530 cm^{-1} (with a very weak shoulder at 1515 cm^{-1}) in 6L PAz. The intensity ratio (within each spectrum) between band at 1566 cm^{-1} and the shoulder around 1530 cm^{-1} drops from 1.54 for 1L to 1.52 for 3L and to 1.41 for 6L PAz. Here, the drop is relatively significant for 6L PAz. When higher to lower excitation energy is used, these bands merge, forming a less intense broad band [27]. The excitation source λ_{exc} = 780 nm provides information on the quinoid units of the film enhancing vibrations arising from doped segments of the film (resonance effect: excitation wavelength coincides with electronic transitions at around 800 nm) [5,27]. In case of AP-VPP PAz, the excitation source is the same; the change is in the number of layers. Therefore, it can be said that 6L PAz has more quinoid form than the 3L and 1L PAz, due to which the relative dispersion in the intensity ratio and the broadening of the bands occur.

Raman spectra of AP-VPP PAz films obtained by using laser excitation wavelength of 785 nm (λ_{exc} = 785 nm) for azulene, 1L, 3L, and, 6L PAz are shown in Fig. 6c and d. The intense sharp band at 1393 cm^{-1} in azulene is observed as a broad, intense band at 1387 cm^{-1} for the PAz film. The other peaks in the azulene spectra are also observed as broad bands at lower frequencies in the PAz film. The band at 1394 cm^{-1} (λ_{exc} = 532 nm) for azulene shifts to 1393 cm^{-1} (λ_{exc} = 785 nm) and the band at 1389 cm^{-1} (λ_{exc} = 532 nm) for PAz shifts to 1387 cm^{-1} (λ_{exc} = 785 nm). When comparing Fig. 6b and d, one can observe that the bands around 1387 cm^{-1} are very intense when λ_{exc} was 785 nm, whereas the bands around 1566 cm^{-1} were intensified when λ_{exc} was 532 nm. It means that the vibrations in the doped form of the PAz are well amplified around 1387 cm^{-1} (by the λ_{exc} = 785 nm or higher), whereas the vibrations in the neutral part of the PAz are well amplified around 1566 cm^{-1} (by the λ_{exc} = 532 nm). The studies reported by Österholm et al. show that the bands in the range 1000–1600 cm^{-1} (λ_{exc} = 780 nm) started to diminish with increase in positive potential (increased p-doping) and completely disappeared at very high potential [27]. This drop in the intensity must be due to the increased polarization effect upon doping at high potential. In Fig. 6c and d, the intensity ratio of the band at 1387 to 1496 cm^{-1} in 6L PAz is 1.05. The intensity ratio of the band at 1387 cm^{-1} to the respective peak for 3L and 1L PAz are 1.72 and 2.25, respectively. The intensity ratio drops in the order 1L > 3L > 6L PAz, which could be due to the polarization effect. The IR data showed that the IR active vibrations became relatively intense in the reverse order (Fig. 5 a). It indicates that the conjugation extends in the reverse order, i.e. 1L < 3L < 6L PAz. The overall shape and intensity of the peaks in 1350 to 1600 cm^{-1} of 1L PAz are relatively different for 3L and very different for 6L PAz. This change indicates varying nature of charge carriers in 1L, 3L, and, 6L PAz structures. This is also observed in the UV–Vis and IR data.

3.5. Surface properties of AP-VPP PAz films by AFM and SEM analysis

In Fig. S2a-c (50 × 50 μm), the surface properties do not change drastically with the additions of layers of PAz whereas, in Fig. 7a–c, the alteration can be visually observed. The number of islands grows and forms denser structure from 1L to 3L and 6L PAz. This observation also stands out in SEM images of 1L and 3L PAz (Fig. 7d–f). These dense aggregates or islands could be the result of cross-linked or long PAz chains. The RMS-roughness values of the films change slightly from 1L (20.7 nm) to 3L (20.9 nm) to 6L PAz (21.3 nm). It appears that the formation of valleys well compensates the dense-island formation; apparently, RMS-roughness is transformed negligibly with the increasing number of layers. In current experimental data, the smoothness of the surface remains roughly unaffected with the increasing number of layers. Although the change in RMS-roughness is insignificant, the electrochemical capacitance of the multi-layered PAz films would provide more insights into the effect of the denser arrangement of the island. AP-VPP-prepared 1L to 6L PEDOT films showed a roughness average within 0.5–3.5 nm range [18]. A quick comparison with this PEDOT signify that the steric hindrance due to the bulky ring component of azulene units lead to the relatively higher roughness for the AP-VPP PAz films.

3.6. Electrochemical characterization of AP-VPP PAz films by cyclic voltammetry

In Fig. 8a–c, as the scan rate is increased the current density clearly increases for all AP-VPP PAz films. It also shows the effect of multiple layers as the current density is highest for 6L PAz. Details for the calculations of areal (C_A) and volumetric capacitance (C_V) of the AP-VPP PAz films are explained in the experimental section. The areal capacitance grow from 1L to 6L PAz due to the addition of electroactive PAz layers. In Fig. 9a, the C_A of 1L, 3L, and, 6L PAz remains quite constant at different scan rates except at 20 mV/s. The slopes of these graphs between 50 and 200 mV/s for 1L, 3L and 6L PAz are 7×10^{-5}, -1.7×10^{-3}, and, -8.4×10^{-3} $mFsmV^{-1}cm^{-2}$, respectively. It indicates that at high scan rate the diffusion-controlled processes are not affected for 1L PAz, slightly affected for 3L PAz, and highly affected for 6L PAz. The drop in C_A at 3L becomes almost six-fold intense for 6 L PAz. This effect can clearly be observed in Fig. 9b. It means that the doping processes for thicker-PAz films are not fast at elevated scan rates. The relation of C_A and C_V with scan rate and film thickness correlate well with sheet resistance and conductivity values. With the number of layers, the sheet resistance does not drop in proportion to the thickness growth. Eventually, with the increasing number of layers conductivity of the PAz films drops with the denser arrangement of the island evidenced in the AFM images. It can be concluded that the denser arrangement of PAz island has a negative effect on the sheet resistance and the capacitance properties. The volumetric capacitances of the PAz films in Fig. 9c and d reveal similar trends. M. Suominen et al. reported electrochemically synthesized PAz in different ionic liquids [6]. These films showed the areal capacitance from 25 to 90 mF/cm^2 [6]. In our work, the 6L PAz exhibited C_A value of 8.3 ± 0.31 mF/cm^2 and C_V of 706.2 ± 140.3 F/cm^3 at 20 mV/s scan rate. The low areal capacitance of 6L PAz compared to M. Suominen et al. reported work could be justified by considering the film thickness. M. Suominen et al. did not report the film thickness. However, by carefully observing the reported SEM images, the electrochemically synthesized PAz films seem to be few micrometers thick [6]. In contrast, in the present work, film thickness remains in the range of 27–147 nm. Both areal and volumetric capacitances obtained in the present work are quite promising when thinking about application as active electrode material of supercapacitors. Also, these values are comparable with the 6L PEDOT film prepared by AP-VPP (10.7 mF/cm^2 and 704 ± 42 F/cm^3) [18].

4. Conclusion

The optimized AP-VPP PAz method enables the processability of PAz with improved properties and is not limited to specific substrate materials. The optical band gap calculation, sheet resistance, %T, and surface roughness analysis provided a platform to optimize an AP-VPP method for PAz films at a nanometer scale. Effect of washing step on the dissolution of oligomers causes a significant increment in sheet resistance of the PAz films except when cell temperature is $\leq$ 45 °C; it shows the inverse effect. The method optimization data provided in the present report allow users to adapt the method according to the applications of PAz and desired properties within the experimental limits can be obtained in the resultant films. Cell temperature lower than 35 °C lead to poor film formation. Transmittance was dropped by 26.3 % when cell temperature was raised from 25 to 95 °C. It dropped by 3.8 % when substrate temperature was raised from 25 to 75 °C, and 1.3 % when polymerization time was extended from 2 to 16 min. The rate of polymer deposition increases with increase in cell temperature. A high rate of polymerization could lead to cross-linking of PAz chains. The restricted doping-induced geometrical changes in highly cross-linked PAz lead to increased sheet resistance values. The roughness comparison with AP-VPP PEDOT [18] signifies a steric hindrance contribution due to the bulky ring component of azulene. The increase in BG and SR confirmed a crowding effect due to the bulky 7-membered ring and extended cross-linking with an increase in polymerization time. A substrate

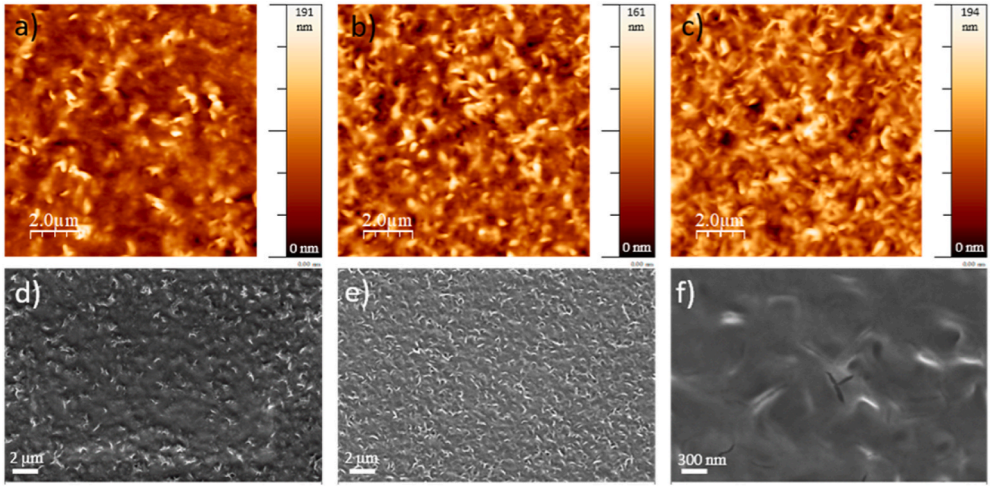

Fig. 7. AFM images of **a)** 1L, **b)** 3L, and **c)** 6L AP-VPP PAz films on glass. SEM images of **d)** 1L and **e-f)** 3L AP-VPP PAz films on glass.

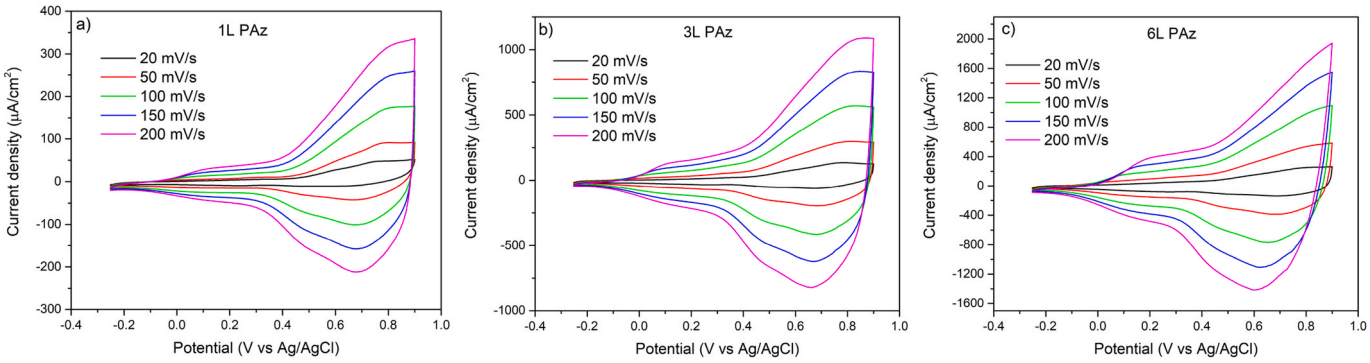

Fig. 8. Cyclic voltammograms in 0.1 M $TBABF_4$/MeCN of **a)** 1L, **b)** 3L, and, **c)** 6L AP-VPP PAz films in the potential range −0.25 V to 0.9 V at various scan rate (mV/s).

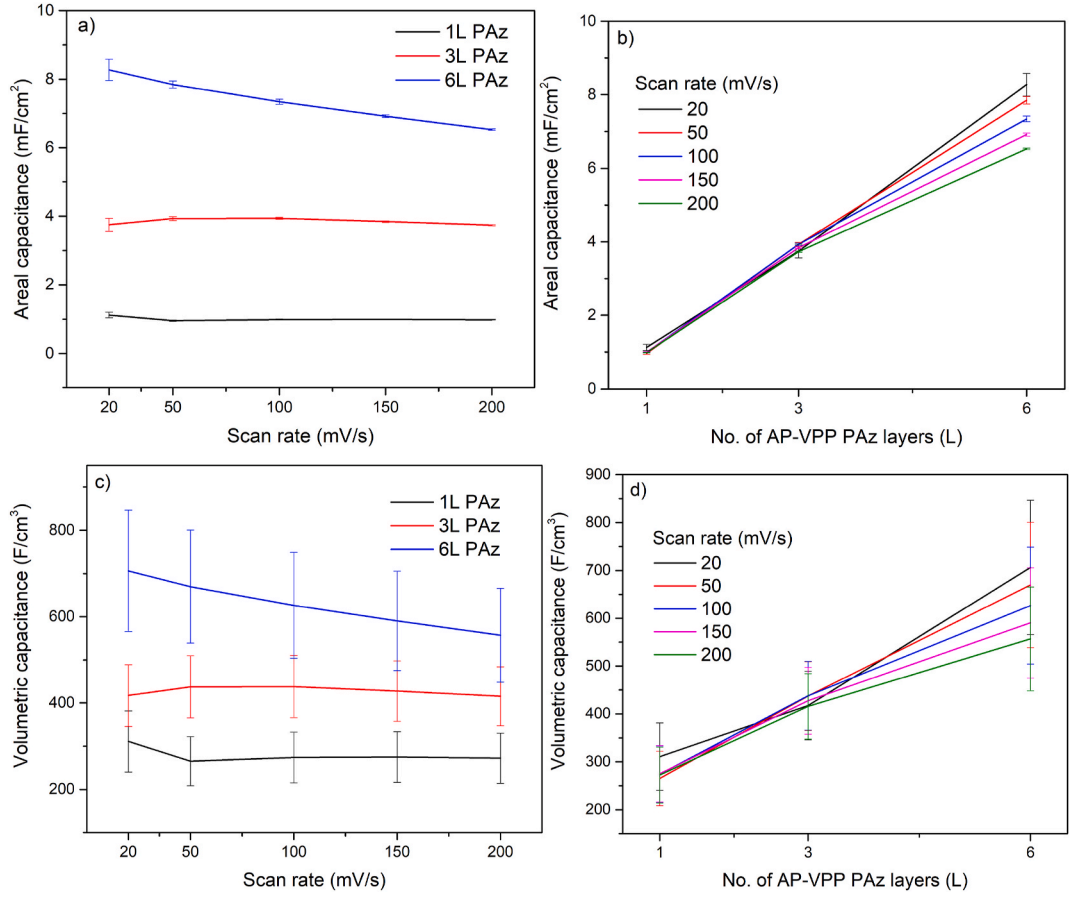

Fig. 9. Behaviour of areal and volumetric capacitances of 1L, 3L, and 6L PAz against **a & c)** scan rate, and **b & d)** number of PAz layers. **(**Error-values (Std Dev and RSD (%)) are provided in Table S2).

temperature control does not substantially improve the PAz film's sheet resistance. The UV–Vis, FTIR, and Raman analysis provided insights into the films' chemical nature. The AP-VPP PAZ films are moderately doped. A red shift of bands originating from radical cation with layers' addition must be the combined effect of growing azulene units in polymer chains and the diminishing linear degree of doping. Two factors explain the anomalous behaviour of PAz: 1. The PAz films would acquire more planar confirmation over distorted nonplanar with the addition of PAz-layers due to the dropping linear degree of doping. 2. Overall doping is improved with the addition of layers indicating an added quinoid form of the multi-layered PAz. It can be concluded from the UV–Vis and NIR data that the proportion of quinoid to neutral form of the PAz is relatively low in 6L PAz compared to 1L, whereas Raman and IR data confirmed that the added quinoid form is higher in 6L than 1L PAz. As a result, the BG and SR drop from 1L to 6L PAz and shifts in IR and Raman spectra are observed. The IR data comparison shows that the order of relative conjugation length is the highest in electrochemically doped Ele-PAz [5] at 1.1V followed by > Ele-PAz [6,12,23] > AP-VPP PAz > Che-PAz [2,7,8]. The dense island formation with the increasing number of layers affected the capacitance properties of the PAz films at very high scan rate. At elevated scan rate, the transport of the dopant ions across the film was unaffected in 1L PAz. It was slightly affected in 3L and notably in 6L PAz. The BG of all the AP-VPP PAz films produced in present work remained in the range of 1.45 to 1.69 eV. Very

high capacitance values indicate promising use of AP-VPP PAz as an electroactive material in batteries and supercapacitors.

CRediT authorship contribution statement

Rahul Yewale: Conceptualization, design of the work, Data collection, Formal analysis, and interpretation, Drafting the article, Critical revision of the article, Final approval of the version to be published. **Pia Damlin:** Conceptualization, design of the work, Critical revision of the article, Final approval of the version to be published. **Milla Suominen:** Critical revision of the article, Final approval of the version to be published. **Carita Kvarnström:** Critical revision of the article, Final approval of the version to be published.

Declaration of competing interest

The authors declare that they have no known competing financial interests or personal relationships that could have appeared to influence the work reported in this paper.

Acknowledgements

The authors thank the Fortum Foundation, Business Finland, and the Jenny and Antti Wihuri Foundation, Finland for financial support. The authors thank Mauri Nauma and Kari Loikas for technical support.

Appendix A. Supplementary data

Supplementary data to this article can be found online at https://doi.org/10.1016/j.matchemphys.2021.125292.

References

[1] K. Iwasaki, K. Matsumoto, S. Hino, Electrochemical polymerization of alkyl-substituted azulene, Synth. Met. 55–57 (1993) 1062–1066.
[2] F. Wang, Y.H. Lai, N.M. Kocherginsky, Y.Y. Kosteski, The first fully characterized 1,3-polyazulene: high electrical conductivity resulting from cation radicals and polycations generated upon protonation, Org. Lett. 5 (2003) 995–998, https://doi.org/10.1021/ol0274615.
[3] Q. Sun, I.C.Y. Hou, K. Eimre, C.A. Pignedoli, P. Ruffieux, A. Narita, R. Fasel, On-surface synthesis of polyazulene with 2,6-connectivity, Chem. Commun. 55 (2019) 13466–13469, https://doi.org/10.1039/c9cc07168g.
[4] T. Hirabayashi, K. Naoi, T. Osaka, Application of electrochemically formed polyazulene to secondary battery, J. Electrochem. Soc. 134 (1987) 758–759, https://doi.org/10.1149/1.2100550.
[5] B. Meana-Esteban, C. Lete, C. Kvarnström, A. Ivaska, Raman and in situ FTIR-ATR characterization of polyazulene films and its derivate, J. Phys. Chem. B 110 (2006) 23343–23350, https://doi.org/10.1021/jp0631811.
[6] M. Suominen, S. Lehtimäki, R. Yewale, P. Damlin, S. Tuukkanen, C. Kvarnström, Electropolymerized polyazulene as active material in flexible supercapacitors, J. Power Sources 356 (2017) 181–190, https://doi.org/10.1016/j.jpowsour.2017.04.082.
[7] K.G. Neoh, E.T. Kang, T.C. Tan, Chemical synthesis and characterization of electroactive and partially soluble polyazulene, Polym. Bull. 19 (1988) 325–331.
[8] E. Grądzka, P. Makowska, K. Winkler, Chemically formed conducting polyazulene: from micro- to nanostructures, Synth. Met. 246 (2018) 115–121, https://doi.org/10.1016/j.synthmet.2018.10.002.
[9] H.D. Burrows, T. Nunes, High resolution solid state NMR evidence for photochemical formation of poly(azulene), Polym. J. 28 (1996) 368–370.
[10] G. Tourillon, F. Garnier, New Electrochemically Generated Organic Conducting Polymers, 1982.
[11] Y. Shim, S. Park, Electrochemistry of conductive polymers: XXII. Electrochemical and spectroelectrochemical studies of polyazulene growth and its characterization, J. Electrochem. Soc. 144 (1997) 3027–3033, https://doi.org/10.1149/1.1837954.
[12] G. Nie, T. Cai, S. Zhang, J. Hou, J. Xu, X. Han, Low potential electrosyntheses of high quality freestanding polyazulene films, Mater. Lett. 61 (2007) 3079–3082, https://doi.org/10.1016/j.matlet.2006.11.004.
[13] E. Grodzka, K. Winkler, B.M. Esteban, C. Kvarnstrom, Capacitance properties of electrochemically deposited polyazulene films, Electrochim. Acta 55 (2010) 970–978, https://doi.org/10.1016/j.electacta.2009.09.054.
[14] G. Nöll, C. Lambert, M. Lynch, M. Porsch, J. Daub, Electronic structure and properties of poly- and oligoazulenes, J. Phys. Chem. C 112 (2008) 2156–2164, https://doi.org/10.1021/jp074376b.
[15] T. Osaka, K. Naoi, T. Hirabayashi, Application of electrochemically formed polyazulene to rechargeable lithium battery, J. Electrochem. Soc. 134 (1987) 2645–2649.
[16] N. He, L. Höfler, R.M. Latonen, T. Lindfors, Influence of hydrophobization of the polyazulene ion-to-electron transducer on the potential stability of calcium-selective solid-contact electrodes, Sensor. Actuator. B Chem. 207 (2015) 918–925, https://doi.org/10.1016/j.snb.2014.10.048.
[17] A. Österholm, B.M. Esteban, C. Kvarnström, A. Ivaska, Spectroelectrochemical study of the redox reactions of polyazulene on aluminum substrates, J. Electroanal. Chem. 613 (2008) 160–170, https://doi.org/10.1016/j.jelechem.2007.10.022.
[18] R. Yewale, P. Damlin, M. Salomäki, C. Kvarnström, Layer-by-layer approach to engineer and control conductivity of atmospheric pressure vapor phase polymerized PEDOT thin films, Mater. Today Commun. 25 (2020), https://doi.org/10.1016/j.mtcomm.2020.101398.
[19] D. Mühlbacher, H. Neugebauer, A. Cravino, N.S. Sariciftci, J.K.J. Van Duren, A. Dhanabalan, P.A. Van Hal, R.A.J. Janssen, J.C. Hummelen, Comparison of electrochemical and spectroscopic data of the low-bandgap polymer ptptb, Mol. Cryst. Liq. Cryst. 385 (2002) 85–92, https://doi.org/10.1080/713738793.
[20] I. Horcas, R. Fernández, J.M. Gómez-Rodríguez, J. Colchero, J. Gómez-Herrero, A. M. Baro, WSXM, A software for scanning probe microscopy and a tool for nanotechnology, Rev. Sci. Instrum. 78 (2007), https://doi.org/10.1063/1.2432410.
[21] K. Iwasaki, H. Tatematsu, Y. Taneda, K. Matsumoto, S. Hino, Temperature and solvents effects on the electrochemical polymerization of azulene, Synth. Met. 69 (1995) 543–544, https://doi.org/10.1016/0379-6779(94)02560-L.
[22] A. Österholm, P. Damlin, C. Kvarnström, A. Ivaska, Studying electronic transport in polyazulene-ionic liquid systems using infrared vibrational spectroscopy, Phys. Chem. Chem. Phys. 13 (2011) 11254–11263, https://doi.org/10.1039/c1cp20246d.
[23] M. Suominen, P. Damlin, C. Kvarnström, Probing the interactions in composite of graphene oxide and polyazulene in ionic liquid by in situ spectroelectrochemistry, Electrochim. Acta 284 (2018) 168–176, https://doi.org/10.1016/j.electacta.2018.07.069.
[24] X. Huang, M.T. Zhao, L. Janiszewska, P.N. Prasad, Surface plasmon study OF electrochemically prepared polymers: polyazulene, Synth. Met. 24 (1988) 245–253.
[25] S. Hino, K. Matsumoto, K. Iwasaki, Photoelectron spectroscopy of a conducting polymer polyazulene, Synth. Met. 41–43 (1991) 793–796, https://doi.org/10.1016/0379-6779(91)91499-Z.
[26] M. Yamada, H. Hagiwara, H. Torigoe, N. Matsumoto, M. Kojima, F. Dahan, J. P. Tuchagues, N. Re, S. Iijima, A variety of spin-crossover behaviors depending on the counter anion: two-dimensional complexes constructed by NH···Cl- hydrogen bonds, [FeIIH3LMe]Cl·X (X = PF 6-, AsF6-, SbF6-, CF3SO3-; H3L Me = tris[2-{[(2methylimi, Chem. Eur J. 12 (2006) 4536–4549, https://doi.org/10.1002/chem.200500972.
[27] A. Österholm, B. Meana-Esteban, C. Kvarnström, A. Ivaska, In situ resonance Raman spectroscopy of polyazulene on aluminum, J. Phys. Chem. B 112 (2008) 6331–6337, https://doi.org/10.1021/jp0762828.